

**Phase-space dynamics of a single-atom laser: Nonclassicality and bistability**A. B. Mikhalychev <sup>\*</sup>, S. V. Vlasenko, and S. Ya. Kilin*B. I. Stepanov Institute of Physics, NAS of Belarus, Nezavisimosti Avenue 68, 220072 Minsk, Belarus* (Received 2 March 2022; revised 8 June 2022; accepted 21 June 2022; published 30 June 2022)

We investigate the dynamics of a single-qubit single-mode laser with continuous incoherent pumping of a qubit, the field mode being initially prepared in a coherent state. Analysis of partial differential equations for quasiprobability distributions helps us distinguish two stages of evolution (coherent and incoherent ones) with their characteristic features. The system can exhibit bistabilitylike behavior, similar to that reported for a single-atom laser with continuous coherent pumping, and is capable of generating Schrödinger cat states. Quantitative analysis of the field state nonclassicality shows that its maximum is reached at intermediate stages of evolution.

DOI: [10.1103/PhysRevA.105.063723](https://doi.org/10.1103/PhysRevA.105.063723)**I. INTRODUCTION**

The single-atom laser represents a simple but important model exhibiting nontrivial dynamics and quantum effects such as Rabi splitting [1–5], collapse and revival of oscillations [6,7], photon blockade [8–11] and its breakdown [12–14], antibunching and sub-Poissonian photon statistics [10,11,15–21], and phase and amplitude bistability [22–24] or multistability [25]. The system can serve as a source of nonclassical field states [26–38] or entangle photons interacting with the atom [10,11,39–43]. Most of the mentioned effects are characteristic even of the simplest single-qubit single-mode model of the laser, while a greater variety of phenomena is predicted for systems with a larger number of engaged atomic energy levels [17,18,37,38,41,44–46], a more complex field structure [10,11,39–43], or additional nonlinearity induced by interaction with a photonic crystal [47–50].

By now, a large number of different approaches have been successfully applied to investigation of the dynamics and the stationary state of a single-atom laser: numerical solution of the master equation for the density operator with the photon-number truncation [18,51–57], approximate semiclassical treatment [18,52,58,59], quantum trajectory approach [35,45,55,59], nonlinear recurrent relations between moments of different orders [60], diagonalization of the Green's operator [53,61], continued fraction expansion [62], Glauber function decomposition in terms of the argument powers or orthogonal polynomials [27,63], or numerical solution of the Fokker-Plank equation in the adiabatic approximation [61]. Analysis of quasiprobability distributions (including Glauber  $P$ , Wigner  $W$ , and Husimi  $Q$  functions) proved to be fruitful and illustrative for investigation of the stationary state [22,27,63–65] and even for prediction of Schrödinger-cat-state generation by a coherently driven single-atom laser at intermediate stages of its evolution [32]. However, thorough and consistent analysis of the single-atom-laser dynamics in

terms of such distributions has not been performed yet but promises to be productive for gaining a better understanding of that fundamental system.

The interest in the single-atom laser has remained strong for a relatively long time due to the gradual development of experimental capabilities for its implementation [15,19,58,66] and the importance of the nonclassical light states for quantum information processing, quantum metrology, imaging, etc. [67–69]. The stationary state of a single-qubit single-mode laser has already been shown to exhibit nonclassical properties for all nontrivial combinations of parameters (all regimes of operation) [18,20,27,33,60]. On the other hand, it is known that nonlinear dissipative systems with pulsed coherent excitation can exhibit more pronounced nonclassical properties at intermediate stages of dynamics relative to the stationary state [70]. That fact, together with the lack of a thorough analysis of the phase-space dynamics of a single-atom laser, motivates us to investigate the behavior of quasiprobability distributions, describing such a system during its quantum evolution, with the aim of getting a more clear understanding of the sources of emerging state nonclassicality and finding the conditions for generating more useful quantum states.

The outline of the paper is as follows. In Sec. II we introduce the considered model of a single-qubit single-mode laser with incoherent pumping of a qubit and provide the differential equations for evolution of  $s$ -ordered quasiprobability distributions. In Sec. III a coherent initial state of the field mode is assumed. A numerical treatment of the phase-space dynamics is presented and divided into two characteristic stages, one coherent and the other incoherent, in Secs. IV and V, respectively. In Sec. VI a typical structure of quasiprobability distributions for the coherent stage is analyzed both numerically and analytically, yielding an analogy with the phase bistability effect [22] and a guess that the Schrödinger-cat states can be generated by the considered single-atom laser. Further, that proposition is proved on the basis of the master equation analysis. The incoherent stage of the dynamics exhibits properties closely related to the amplitude bistability of a coherently pumped single-atom laser. In Sec. VII we provide quantitative analysis of the

<sup>\*</sup>mikhalychev@gmail.com

nonclassicality of the generated field state and discuss the conditions maximizing it.

## II. MODEL

### A. Master equation

In the present research, we consider a model of a single-qubit single-mode laser with incoherent pumping. A two-level atom with the ground state  $|1\rangle$  and the excited state  $|2\rangle$  interacts with a resonance field mode with the coupling constant  $g$ . Incoherent pumping of the atom with the mean rate  $R_{12}$ , decay of the excited states of the field mode and the atom, and dephasing of the atom with the rates  $\kappa$ ,  $R_{21}$ , and  $\Gamma$ , respectively, are taken into account. The dynamics of the density operator  $\rho$  of the considered model system is described by the master equation in the interaction representation

$$\begin{aligned} \frac{d}{dt}\rho = & -\frac{i}{\hbar}[H, \rho] + 2\kappa\mathcal{L}(a)\rho \\ & + R_{12}\mathcal{L}(\sigma_+)\rho + R_{21}\mathcal{L}(\sigma_-\rho) + \Gamma\mathcal{L}(\sigma_z)\rho, \end{aligned} \quad (1)$$

where the operators  $\sigma_-$ ,  $\sigma_+$ ,  $\sigma_z$  and  $a$ ,  $a^\dagger$  describe the dynamics of the atom and the field, respectively. The relaxation is represented in the Lindblad form  $2\mathcal{L}(X)\rho = 2X\rho X^\dagger - X^\dagger X\rho - \rho X^\dagger X$ . The interaction Hamiltonian  $H$  corresponds to the Jaynes-Cummings model [71]

$$H = g\hbar(a^\dagger\sigma_- + a\sigma_+). \quad (2)$$

It is convenient to use the following normalized parameters characterizing the system [27,33]: the relative incoherent pump rate  $a_0^2 = R_{12}/4\kappa$ , the normalized difference between the atom and the field decay rates  $v_0 = (R_{21} - 2\kappa)/4\kappa$ , the relative decoherence rate  $\mu_0 = a_0^2 + v_0 + \Gamma/\kappa$ , and the normalized strength of the unitary atom-field interaction  $\eta = g^2/\kappa^2$ . In terms of the introduced parameters, the condition  $R_{12} > R_{21}$ , indicating that the incoherent pump tends to create population inversion, takes the form  $v_0 - a_0^2 < -\frac{1}{2}$ .

The density operator of the considered system can be decomposed over the states of the atom as

$$\begin{aligned} \rho = & \rho_{11} \otimes |1\rangle\langle 1| + \rho_{22} \otimes |2\rangle\langle 2| + i\rho_{21} \otimes |2\rangle\langle 1| \\ & - i\rho_{12} \otimes |1\rangle\langle 2|, \end{aligned} \quad (3)$$

where the factor  $i$  is introduced to make further equations simpler; the equality  $\rho_{21} = \rho_{12}^\dagger$  holds. Then the master equation (1) can be transformed into the following set of equations for the components of the density operator:

$$\begin{aligned} \frac{1}{\kappa} \frac{d}{dt} \rho_{11} = & (2J - N - N' - 4a_0^2)\rho_{11} + (4v_0 + 2)\rho_{22} \\ & + \sqrt{\eta}(a^\dagger\rho_{21} + \rho_{12}a), \end{aligned} \quad (4)$$

$$\begin{aligned} \frac{1}{\kappa} \frac{d}{dt} \rho_{22} = & (2J - N - N' - 4v_0 - 2)\rho_{22} + 4a_0^2\rho_{11} \\ & - \sqrt{\eta}(a\rho_{12} + \rho_{21}a^\dagger), \end{aligned} \quad (5)$$

and

$$\begin{aligned} \frac{1}{\kappa} \frac{d}{dt} \rho_{12} = & (2J - N - N' - 2\mu_0 - 1)\rho_{12} \\ & - \sqrt{\eta}\rho_{11}a^\dagger + \sqrt{\eta}a^\dagger\rho_{22}. \end{aligned} \quad (6)$$

Here the superoperators of quantum jumps ( $J$ ) and the numbers of photons ( $N$  and  $N'$ )

$$J\rho \doteq a\rho a^\dagger, \quad N\rho \doteq a^\dagger a\rho, \quad N'\rho \doteq \rho a^\dagger a \quad (7)$$

were introduced.

Further, we assume that the initial state of the system is described by the expression

$$\rho(0) = |\alpha_0\rangle\langle\alpha_0| \otimes |1\rangle\langle 1|, \quad (8)$$

with the atom being in the ground state and the field being in the coherent state  $|\alpha_0\rangle$ . For the initial state (8), the components have the following values:

$$\rho_{11}(0) = |\alpha_0\rangle\langle\alpha_0|, \quad \rho_{22}(0) = \rho_{12}(0) = \rho_{21}(0) = 0. \quad (9)$$

### B. Phase-space representation

For an illustrative representation of the dynamics of a single-atom laser, as well as for a quantitative description of its nonclassical properties, it is convenient to use the  $s$ -ordered quasiprobability distribution  $P(\alpha; s)$ , defined as the expectation value of the operator [72,73]

$$\delta(a - \alpha; s) \doteq \frac{2}{\pi(1-s)} \exp\left(-\frac{2(a^\dagger - \alpha^*)(a - \alpha)}{1-s}\right), \quad (10)$$

where the columns denote normal ordering of operators of creation and annihilation. Such  $s$ -ordered quasiprobability distributions  $P(\alpha; s)$  represent smoothed versions of the Glauber  $P$  function  $P(\alpha)$  [72],

$$P(\alpha; s) = \frac{2}{\pi(1-s)} \int d^2\gamma P(\gamma) \exp\left(-\frac{2|\alpha - \gamma|^2}{1-s}\right), \quad (11)$$

and are well behaved for  $s \leq s_R$ , where the critical value  $s_R \leq 1$  depends on the nonclassicality of the represented quantum state, even if the Glauber function is singular.

The phase-space representation, based on  $s$ -ordered quasiprobability distributions, is especially convenient for the description of the dynamics of an incoherently pumped single-qubit laser, since its stationary state is known to be characterized by a singular Glauber function in any nontrivial regime [33], while the quasiprobability distribution  $P(\alpha; s)$  is regular for any  $s < 1$  (Appendix A). An additional useful property of quasiprobability distributions is their close connection to the definition of the state nonclassicality according to semipositiveness of the Glauber function [74,75]. The nonclassicality depth  $\tau$  of the field state  $\rho$  can be characterized by the minimal (critical) value  $s_c$  of the parameter  $s$ , for which the function  $P(\alpha; s)$  is not strictly positive [76,77]:

$$\tau = \frac{1 - s_c}{2}, \quad s_c = \inf\{s \mid \exists \alpha : \text{Tr}[\rho\delta(a - \alpha; s)] \leq 0\}. \quad (12)$$

The value  $\tau$  should be used for quantification of the state nonclassicality with caution, since it is a discontinuous function of  $\rho$  [77]. On the other hand, it provides a reasonable tool for characterizing nonclassicality both of the stationary state of a single-qubit laser [33] and of interim states of its dynamics (discussed below). Other common approaches to nonclassicality quantification and detection (negativity of the

Mandel parameter [75] and Wigner function [76,77], dominance of odd photon numbers [78], breaking of non-negativity of quadrature moments in quadratic form [79,80], or ordering sensitivity [81]) fail when applied to the stationary state of a single-qubit laser in certain regimes where the state is known to be nonclassical [33]. Such approaches are not expected to provide a reasonable description of nonclassicality of the single-qubit laser dynamics.

The set of equations (4)–(6) can be transformed into differential equations for  $s$ -ordered quasiprobability distributions

$$\begin{aligned} P_{11}(\alpha; s) &= \text{Tr}\{\rho_{11}\delta(a - \alpha; s)\}, \\ P_{22}(\alpha; s) &= \text{Tr}\{\rho_{22}\delta(a - \alpha; s)\}, \\ P_{\text{Re}}(\alpha; s) &= \text{Tr}\left\{\frac{\rho_{12} + \rho_{21}}{2}\delta(a - \alpha; s)\right\}, \\ P_{\text{Im}}(\alpha; s) &= \text{Tr}\left\{\frac{\rho_{12} - \rho_{21}}{2i}\delta(a - \alpha; s)\right\} \end{aligned} \quad (13)$$

by applying the rules for mapping creation and annihilation operators acting on density operators onto differential phase-space operators [82]. The combinations of the operators  $\rho_{12}$  and  $\rho_{21}$  are chosen to ensure that the resulting operators are Hermitian. The resulting partial differential equation takes the form

$$\frac{1}{\kappa} \frac{d}{dt} u = c \Delta u + \nabla \cdot (\boldsymbol{\gamma} u) - (\boldsymbol{\beta} \cdot \nabla) u - a u, \quad (14)$$

where  $u = (P_{11}(\alpha; s), P_{22}(\alpha; s), P_{\text{Re}}(\alpha; s), P_{\text{Im}}(\alpha; s))^T$  is a four-component column vector composed of quasiprobability distributions, the derivative operators  $\nabla = (\partial/\partial x, \partial/\partial y)^T$  and  $\Delta = \nabla \cdot \nabla = \partial^2/\partial x^2 + \partial^2/\partial y^2$  refer to the coordinates  $x = \text{Re } \alpha$  and  $y = \text{Im } \alpha$ ,  $c = (1 - s)/4$  is a scalar diffusion coefficient, and a two-component vector  $\boldsymbol{\gamma} = (x, y)^T$  represents the conservative flux coefficient. The explicit expressions for the convection coefficient  $\boldsymbol{\beta}$  (a  $4 \times 4$  matrix with each element being a two-component vector) and the absorption coefficient  $a$  (a  $4 \times 4$  matrix with scalar elements) are listed in Appendix B.

To solve Eq. (14) numerically, we apply the finite-element method [83] to a truncated region of the phase space. The considered region is selected in a way ensuring that the quasiprobability distributions take small values [ $|P(\alpha; s)| < 10^{-3}$ ] outside it throughout the modeling process. For example, for the initial state (8) with  $\alpha_0 = 10$  it is sufficient to consider the region  $x \in [-3, 12]$  and  $y \in [-4, 4]$ . Additionally, we impose the zero-flux boundary condition

$$\boldsymbol{n} \cdot (c \nabla u + \boldsymbol{\gamma} u) = 0, \quad (15)$$

where  $\boldsymbol{n}$  is the vector normal to the boundary of the analyzed region, to preclude flow of the quasiprobability away from the region.

For additional speedup of numerical calculations, it is useful to take into account the following symmetry of Eqs. (14) and (15) relative to orthogonal transformations (rotation or reflection) of the phase space:  $(x, y)^T \mapsto O(x, y)^T$ . If the vector  $u$  is transformed as

$$u \mapsto \begin{pmatrix} I & 0 \\ 0 & O \end{pmatrix} u, \quad (16)$$

where  $I$  is the  $2 \times 2$  identity matrix, Eqs. (14) and (15) preserve their form for the new coordinates and the new vector of quasiprobability distributions  $u$ . The symmetry arises from the phase invariance of the master equation (1) with an incoherent pump. Therefore, without loss of generality, one can assume that the amplitude of the initial coherent state  $|\alpha_0\rangle$  is a real non-negative number  $\alpha_0 \geq 0$ . The solution for any other initial state of the form (8) can be obtained by applying the corresponding rotation transformation  $O$ .

For a real-value amplitude of the initial coherent state, both the equations and the initial conditions possess the symmetry relative to reflection around the real axis  $x$  ( $y \mapsto -y$  and  $\alpha \mapsto \alpha^*$ ):

$$\begin{aligned} P_z(\alpha^*; s) &= P_z(\alpha; s), \quad z = 11, 22, \text{Re} \\ P_{\text{Im}}(\alpha^*; s) &= -P_{\text{Im}}(\alpha; s). \end{aligned} \quad (17)$$

Therefore, the symmetry relations (17) are satisfied for the dynamics of the considered system and can be used for a twofold reduction of the number of nodes in the mesh, constructed for solving Eq. (14). Only the region  $y \geq 0$  is to be considered, while the values for  $y < 0$  can be recovered according to Eq. (17).

### III. PHASE-SPACE DYNAMICS

To identify typical regimes of the considered single-qubit laser dynamics, we start from its numerical modeling. A mesh consisting of 17 668 domain elements and 354 boundary elements is used to solve the partial differential equation (14). Figure 1 shows the characteristic behavior of the quasiprobability distribution function  $P_{11}(\alpha; s) + P_{22}(\alpha; s)$ , corresponding to the field state after tracing out the atom:  $\rho_{\text{field}} = \text{Tr}_{\text{atom}} \rho$ . The results are shown for the regime without population inversion [model 1:  $\nu_0 - a_0^2 > -\frac{1}{2}$ , Fig. 1(a)] and for incoherent excitation tending to create population inversion [model 2:  $\nu_0 - a_0^2 < -\frac{1}{2}$ , Fig. 1(b)]. The value  $s = 0.5$  of the ordering parameter, used for the simulation, provides the optimal trade-off between sensitivity of the quasiprobability distributions and numerical stability of their modeling and representation (Appendix C). For both parameters sets (as well as for many other sets used for modeling but not shown in Fig. 1), one can see a qualitatively different shape of the quasiprobability distribution at different stages of the dynamics.

There exist two essential features for the initial stage of evolution: a strong phase dependence, pointing to retention of coherent properties of the state, and the presence of an interference region with negative values of the quasiprobability distribution function, which points to the essentially nonclassical properties of the state. This stage corresponds to a significant excess of an average number of photons  $\langle n \rangle$  over the stationary state value  $a_0^2$  and can be reached only for a sufficiently intense initial state of the field:  $|\alpha|^2 \gg a_0^2$ . Further, we show that such a coherent stage can exhibit a close analog of phase bistability, predicted in Ref. [22] and observed in Ref. [23], and generates a Schrödinger-cat field state.

The other stage is characterized by  $\langle n \rangle \sim a_0^2$  and corresponds to the system approaching the stationary state. The

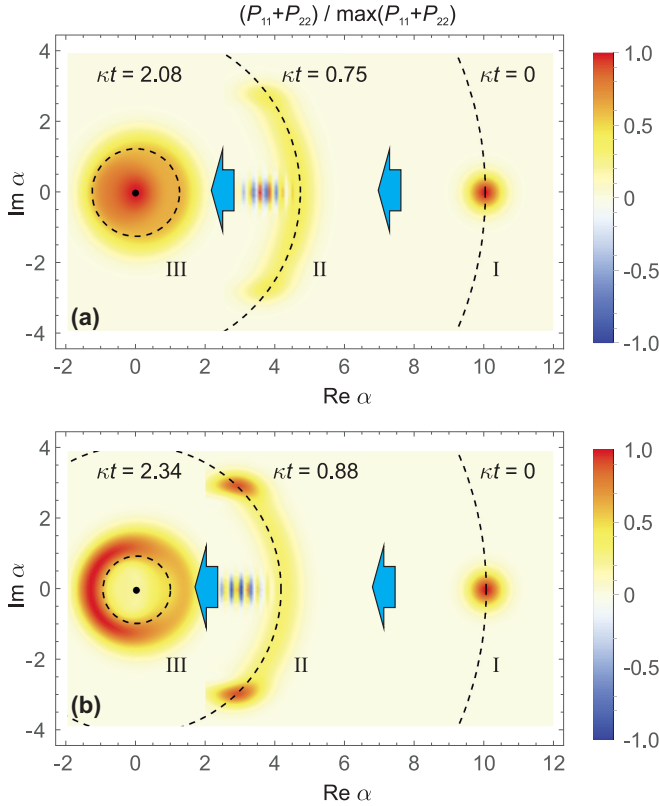


FIG. 1. Overlaid quasiprobability distributions  $P_{11}(\alpha; s) + P_{22}(\alpha; s)$  for different stages of the single-qubit laser dynamics: initial coherent state I, coherent stage II, and incoherent stage III. The results are shown for (a)  $\alpha_0 = 10$ ,  $a_0^2 = 1.0$ ,  $\eta = 1.3 \times 10^2$ ,  $v_0 = 1.0$ , and  $\mu_0 = 2.0$  (model 1) and (b)  $v_0 = -0.31$  and  $\mu_0 = 0.69$  (model 2). The quasiprobability distributions are normalized by their maximal values and correspond to  $s = 0.5$  (i.e., the ordering parameter  $s$  is in the middle between  $s = 0$  for the Wigner function and  $s = 1$  for the Glauber function). Dashed lines indicate the field amplitude decay  $\alpha_0 e^{-\kappa t}$  without the atom-field interaction and are shown for visual guidance.

shape of the quasiprobability distribution differs in Figs. 1(a) and 1(b): Depending on the parameters, the most probable field amplitude of the stationary state can have either a zero (thermal regime, model 1) or nonzero value (lasing regime, model 2). However, for both cases the phase information about the initial coherent state is practically lost; the stage can be termed incoherent. The obtained field states are expected to possess essentially fewer nonclassical properties than in the high-amplitude regime and therefore are less useful for quantum information and metrology applications. Nevertheless, this regime is worth studying further since it can exhibit an effect close to the amplitude bistability effects discovered in Refs. [12,13,22].

#### IV. COHERENT STAGE

##### A. Substages and characteristic regions

The coherent stage of the dynamics starts from the initial coherent state with high amplitude  $\alpha_0 \gg a_0$  and includes the formation of a superposition of coherent states with strong

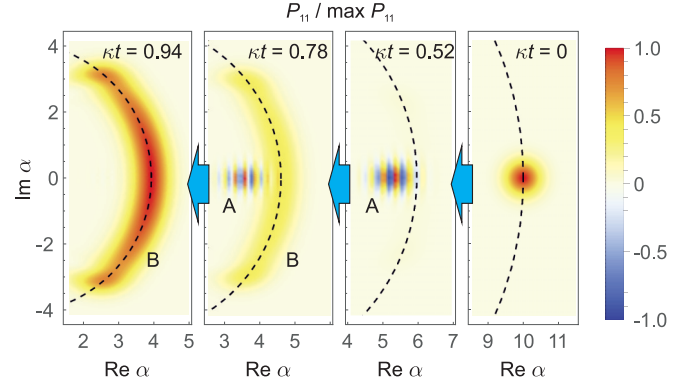


FIG. 2. Coherent stage of the single-qubit laser dynamics. The initial coherent state is transformed into a highly nonclassical Schrödinger-cat state with an intense interference region A. The quantum coherence of the state decays due to dissipative interaction with the environment. An arc B corresponds to a mixture of coherent states, generated after the decay of interference. The quasiprobability distribution function  $P_{11}(\alpha; s)$ , conditioned by the ground state of the atom, is shown. The simulation parameters correspond to model 1 and are the same as in Fig. 1(a).

nonclassicality (Schrödinger-cat states) and then damping of quantum interference with the transition to the state close to a classical mixture of coherent states. Figure 2 illustrates those substages.

The quasiprobability distributions, describing the field state during the coherent stage, have two characteristic regions: the interference region A (Fig. 2), which is formed by the normalized time  $\kappa t_f \sim 1/\sqrt{\eta}$  (discussed below) and decays in  $\kappa t_d \sim 1/(a_0^2 + v_0 + \frac{1}{2})$ , and the arc B, describing the phase distribution of the coherent states, contributing to the decomposition of the field state and having the absolute values of the amplitudes  $|\alpha| \approx \alpha_0 e^{-\kappa t}$ . The two-region structure is preserved over the entire duration of the coherent stage of dynamics, but the interference region is negligible outside the time period  $\kappa t_f \lesssim \kappa t \lesssim \kappa t_d$ . Since the interference region A and the arc B have significantly different structure in the phase space, it is worth considering them in more detail separately.

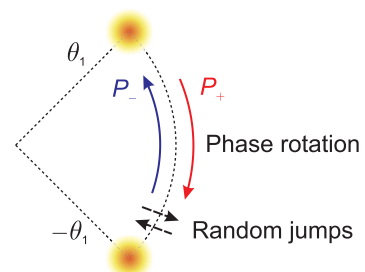


FIG. 3. Interpretation of Eq. (20) in the form of phase rotation (in the clockwise direction for the distribution  $P_+$  and in the counterclockwise direction for  $P_-$ ) and random jumps between the two states.

### B. Arc region

For the regimes when the coherent stage of dynamics is observed, the following conditions typically hold:  $\eta \gg 1$  and  $\langle n \rangle \gg 1$ . The arc region is additionally characterized by relatively slow variations of the quasiprobability distributions with the time  $t$  and the coordinates  $x$  and  $y$ . To describe that region, it is convenient to use the polar coordinates ( $r$  and  $\theta$ ):  $\alpha = re^{i\theta}$ ,  $x = r \cos \theta$ , and  $y = r \sin \theta$ , where  $r \gg 1$  for the arc region.

The leading term of Eq. (14) relative to the discussed large quantities is proportional to  $\sqrt{\eta}r$  and requires the following conditions to be fulfilled to ensure small enough values of  $\partial P_z / \partial t$ ,  $z = 11, 22, \text{Re}, \text{Im}$  (Appendix D):

$$\begin{aligned} P_{22}(\alpha; s) - P_{11}(\alpha; s) &= O\left(\frac{1}{r}, \frac{1}{\sqrt{\eta}}\right), \\ P_{\text{Re}}(\alpha; s) \cos \theta - P_{\text{Im}}(\alpha; s) \sin \theta &= O\left(\frac{1}{r}, \frac{1}{\sqrt{\eta}}\right). \end{aligned} \quad (18)$$

The constraints (18) imply that the dynamics of the arc region is primarily described by just two independent quasiprobability distributions, which can be selected as (see Appendix D)

$$P_{\pm}(\alpha; s) = P_{11} \pm \frac{P_{\text{Im}}}{\cos \theta}. \quad (19)$$

The introduced combinations of quasiprobability distributions satisfy the following system of differential equations:

$$\frac{1}{\kappa} \frac{\partial}{\partial t} P_{\pm} \approx L_r P_{\pm} \pm \frac{\sqrt{\eta}}{2r} \frac{\partial}{\partial \theta} P_{\pm} - \left(\mu_0 + \frac{1}{2}\right) (P_{\pm} - P_{\mp}). \quad (20)$$

Here the radial operator  $L_r$  describes the drift of the quasiprobability distributions to the origin  $\alpha = 0$  due to the field decay

$$L_r P_{\pm} = \frac{1}{r} \frac{\partial}{\partial r} (r^2 P_{\pm}) + \frac{1-s}{4} \left( \frac{\partial^2 P_{\pm}}{\partial r^2} + \frac{1}{r} \frac{\partial P_{\pm}}{\partial r} \right) \quad (21)$$

and is the same for  $P_+$  and  $P_-$ . The most probable amplitude for the arc region of quasiprobability distributions moves according to  $r(t) = \alpha_0 e^{-\kappa t}$ .

The remaining part of Eq. (20) can be interpreted as angular (phase) rotation in the clockwise direction for the distribution  $P_+$  and in the counterclockwise direction for  $P_-$  with the angular speed  $\sqrt{\eta}/2r$  and random jumps between the two clockwise and counterclockwise states described by  $P_+$  and  $P_-$ , respectively, with the rate  $\mu_0 + \frac{1}{2}$  (Fig. 3). For the moment, we limit our consideration of the dynamics by the phase-space quasiprobability distributions, while its interpretation in terms of corresponding state vectors is discussed below.

In the strong-coupling regime  $\sqrt{\eta} \gg \mu_0 + \frac{1}{2}$ , the rotation terms play the main role and the solution is represented by two

peaks near the points

$$\theta = \pm \theta_1, \quad \theta_1 = \frac{\sqrt{\eta}}{2\alpha_0} \{\exp(\kappa t) - 1\}. \quad (22)$$

This result is very close to the effect of the phase bistability of a single-atom laser with coherent pumping found in Refs. [22,23]. In our case, an intense coherent state, initially injected in the resonator of the single-qubit laser, efficiently represents a coherent pump. This similarity can be seen by explicitly introducing the coherent displacement operator  $D(\alpha_0) = e^{\alpha_0(a^\dagger - a)}$  into the master equation (1),  $\rho = D(\alpha_0) \tilde{\rho} D^\dagger(\alpha_0)$ ,

$$\begin{aligned} \frac{d}{dt} \tilde{\rho} &= -\frac{i}{\hbar} [H + \Delta H(\alpha_0), \tilde{\rho}] + 2\kappa \mathcal{L}(a) \tilde{\rho} \\ &+ R_{12} \mathcal{L}(\sigma_+) \tilde{\rho} + R_{21} \mathcal{L}(\sigma_-) \tilde{\rho} + \Gamma \mathcal{L}(\sigma_z) \tilde{\rho}, \end{aligned} \quad (23)$$

where  $\Delta H(\alpha_0) = g\hbar\alpha_0(\sigma_- + \sigma_+) + i\kappa\hbar\alpha_0(a - a^\dagger)$  is the addition to the Hamiltonian describing effective coherent driving of the atom and the field mode, similar to the one considered in Ref. [22].

In the strong loss regime  $\sqrt{\eta} \ll \mu_0 + \frac{1}{2}$ , the effect of bistability is not observed and the angular dependence of functions of the quasiprobability distribution corresponds to a random walk with the half-width of the covered angular region being equal to

$$\theta_2 = \sqrt{\frac{\eta[\exp(2\kappa t) - 1]}{(8\mu_0 + 4)\alpha_0}}. \quad (24)$$

In Fig. 4, examples of quasiprobability distribution functions for the described situations are presented: a random walk [Fig. 4(a)] and bistability [Fig. 4(b)].

### C. Interference region

The interference region differs from the arc by rapid oscillations of quasiprobability distributions:  $\partial P_z / \partial x = O(\sqrt{\eta})$ ,  $z = 11, 22, \text{Re}, \text{Im}$  (Appendix E). The leading order of the decomposition of Eq. (14) over the large parameters includes terms proportional to  $\eta$  and  $\sqrt{\eta}x$ , where we take into account that  $x \sim \langle n \rangle \gg 1$  for the considered region:

$$\frac{1}{\kappa} \frac{\partial P_{11}}{\partial t} \approx x \frac{\partial P_{11}}{\partial x} - \sqrt{\eta} \frac{1+s}{4} \frac{\partial P_{\text{Re}}}{\partial x} + 2\sqrt{\eta} x P_{\text{Re}}, \quad (25)$$

$$\frac{1}{\kappa} \frac{\partial P_{22}}{\partial t} \approx x \frac{\partial P_{22}}{\partial x} - \sqrt{\eta} \frac{1-s}{4} \frac{\partial P_{\text{Re}}}{\partial x} - 2\sqrt{\eta} x P_{\text{Re}}, \quad (26)$$

$$\begin{aligned} \frac{1}{\kappa} \frac{\partial P_{\text{Re}}}{\partial t} &\approx x \frac{\partial P_{\text{Re}}}{\partial x} - \sqrt{\eta} \frac{1-s}{4} \frac{\partial P_{11}}{\partial x} \\ &- \sqrt{\eta} \frac{1+s}{4} \frac{\partial P_{22}}{\partial x} - \sqrt{\eta} x P_{11} + \sqrt{\eta} x P_{22}, \end{aligned} \quad (27)$$

$$\frac{1}{\kappa} \frac{\partial P_{\text{Im}}}{\partial t} \approx x \frac{\partial P_{\text{Im}}}{\partial x}. \quad (28)$$

The obtained system of differential equations can be split into two independent parts: Eq. (28) can be treated separately and yields  $P_{\text{Im}} \approx 0$  in the interference region since  $P_{\text{Im}} = 0$  for  $t = 0$ . The solution of Eqs. (25)–(27) can be found in the form

$$\begin{aligned} P_z(x, y, t) &= A(x, y, t) b_z \cos(\omega t + kx + \varphi_z), \\ z &= 11, 22, \text{Re}, \end{aligned} \quad (29)$$

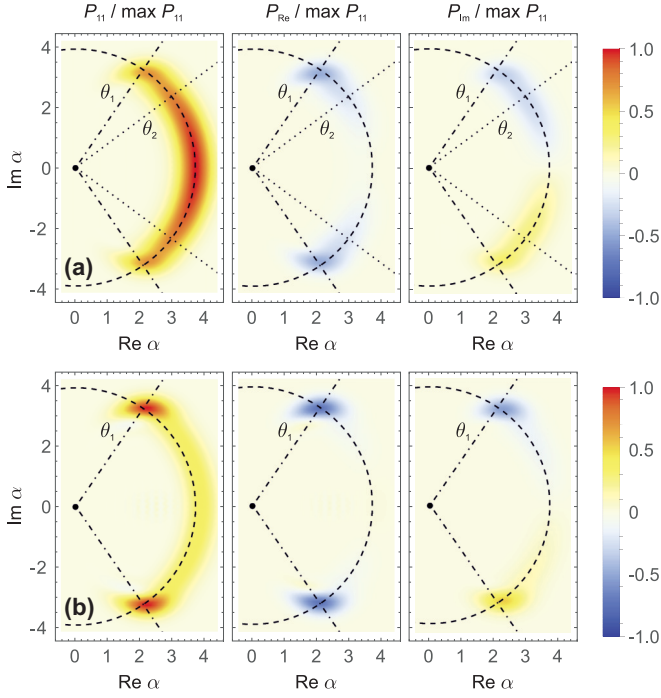


FIG. 4. Quasiprobability distributions for the arc region of the coherent stage of dynamics: (a) a random walk for strong losses and (b) bistability for strong coupling. The simulation parameters are the same as for the corresponding panels of Fig. 1 and describe models 1 and 2, respectively. The quasiprobability distributions  $P_{11}$ ,  $P_{\text{Re}}$ , and  $P_{\text{Im}}$  are shown for  $\kappa t = 1.0$  and normalized by  $\max P_{11}$ . The function  $P_{22}$  is not shown since it equals  $P_{11}$  with high accuracy. Dot-dashed and dotted lines show the directions provided by Eqs. (22) and (24), respectively.

where  $A_z(x, y, t)$  is a slowly varying envelope amplitude and the oscillation parameters can be approximated as

$$k \approx \frac{2\sqrt{\eta}s}{\sqrt{1-3s+3s^2}}, \quad \omega \approx (3k + \sqrt{16\eta - 3k^2}) \frac{\kappa x}{2}; \quad (30)$$

the expressions for the relative amplitudes  $b_z$  and phases  $\varphi_z$  are listed in Appendix E.

Figure 5 shows an example of quasiprobability distributions in the oscillations region. As expected from an approximate analytical treatment,  $P_{\text{Im}}$  takes more than 15 times smaller values relative to other conditional quasiprobability distributions. The expressions, given in Appendix E, predict the ratio of oscillation amplitudes  $b_{11}:b_{22}:b_{\text{Re}} \approx 1.6:1.0:1.0$  for the simulation parameters, used in Fig. 5. The relative phases are  $\varphi_{11} - \varphi_{\text{Re}} \approx 119^\circ$  and  $\varphi_{22} - \varphi_{\text{Re}} \approx -143^\circ$ . All the discussed predictions agree with the results of numerical simulations.

The envelope amplitude  $A(x, y, t)$  can be found by considering next orders of the decomposition. However, the observed structure composed of the arc and interference regions closely resembles a quasiprobability distribution of a Schrödinger-cat state

$$|\Psi_{\text{cat}}\rangle \propto |\xi + i\chi\rangle + e^{i\varphi} |\xi - i\chi\rangle, \quad (31)$$

where the two coherent states  $|\xi \pm i\chi\rangle$  possess the same real part of the amplitude  $\xi$  and opposite imaginary parts  $\pm\chi$ .

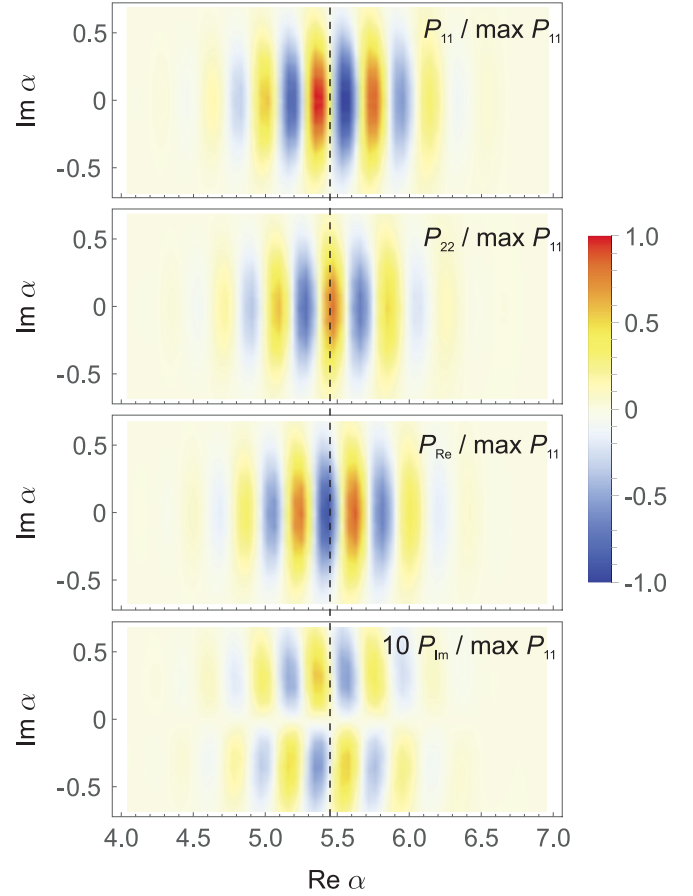


FIG. 5. Quasiprobability distributions for the interference region of the coherent stage of dynamics: from top to bottom  $P_{11}$ ,  $P_{22}$ ,  $P_{\text{Re}}$ , and  $P_{\text{Im}}$ . For  $P_{\text{Im}}$ , ten-times-larger values are shown. The simulation parameters correspond to model 1 and are the same as in Fig. 1(a). The quasiprobability distributions are shown for  $\kappa t = 0.49$  and normalized by  $\max P_{11}$ . The dashed line serves as visual guidance during the comparison of relative oscillation phases.

The corresponding quasiprobability distribution is described by the expression

$$\begin{aligned} P(\alpha; s) \propto & \exp\left(-2\frac{(x-\xi)^2 + (y-\chi)^2}{1-s}\right) \\ & + \exp\left(-2\frac{(x-\xi)^2 + (y+\chi)^2}{1-s}\right) \\ & + 2\exp\left(-2\frac{(x-\xi)^2 + y^2 - s(\xi^2 + \chi^2)}{1-s}\right) \\ & \times \cos\left(\frac{4x\beta}{1-s} - \varphi\right), \end{aligned} \quad (32)$$

where the first two terms form two peaks similar to the ones observed in the bistability regime, while the last term represents the interference region. Figure 6 shows the result of fitting the conditional field state  $\rho_{11}$ , corresponding to the ground state of the atom, by a Schrödinger-cat state with variable parameters  $\xi$ ,  $\chi$ , and  $\varphi$  (Appendix F). The results demonstrate the relatively high fidelity of such a representation for  $\kappa t \lesssim 0.1$ . Therefore, it is instructive to consider

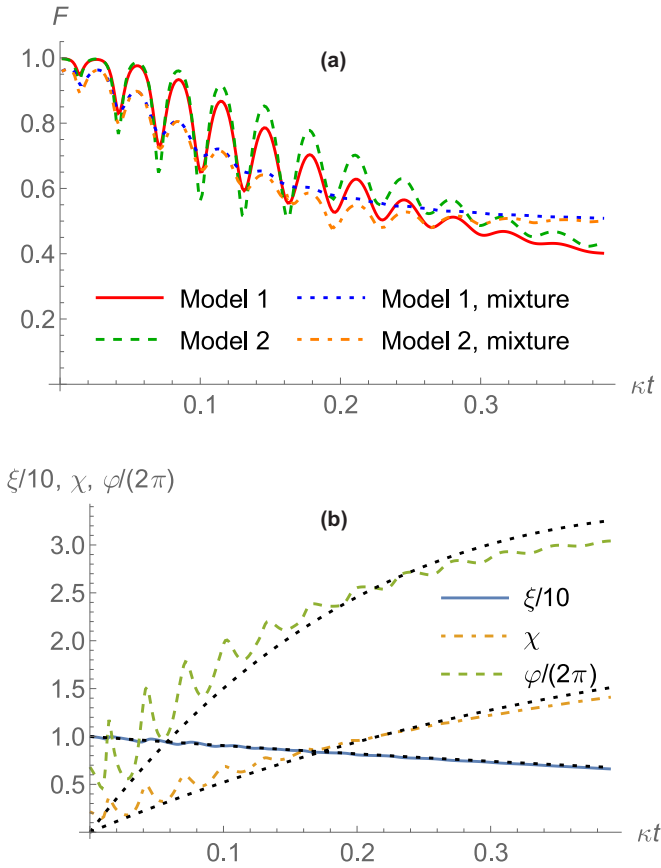


FIG. 6. Representation of the conditional field state  $\rho_{11}$ , corresponding to the ground state of the qubit, as a Schrödinger-cat state (31). (a) Fidelity of representation for model 1 (red solid line) and model 2 (green dashed line). For visual guidance, the fidelity of approximating the Schrödinger-cat state by a mixture of two coherent states with the corresponding amplitudes is shown by the blue dotted line (model 1) and the orange dot-dashed line (model 2). (b) Best-fit parameters of the Schrödinger-cat states, defined according to Eq. (31):  $\xi/10$  (blue solid line),  $\chi$  (orange dot-dashed line), and  $\varphi/2\pi$  (green dashed line). Black dotted lines show the approximate values of those parameters according to Eq. (42).

the shape of the quasiprobability distributions from that perspective, similarly to the analysis of a coherently pumped single-atom laser reported in Ref. [32].

#### D. Schrödinger-cat-state generation

The structure of the quasiprobability distributions resembles the one, described by Eq. (32), when the conditions of an intense field ( $\langle n \rangle \gg 1$ ) and strong coupling ( $\eta \gg 1$  and  $\sqrt{\eta} \gg \mu_0 + \frac{1}{2}$ ) are fulfilled. In that case, the dynamics of the quantum state will be mostly defined by the interaction Hamiltonian (2), which has the eigenvectors [71]

$$|\Psi_{n,\pm}\rangle = (|n+1, 1\rangle \pm |n, 2\rangle)/\sqrt{2}, \quad |\Psi_0\rangle = |0, 1\rangle \quad (33)$$

and corresponding eigenvalues

$$E_{n,\pm} = \pm \hbar g \sqrt{n+1}. \quad (34)$$

One can construct projectors onto three orthogonal subspaces using the eigenvectors (33):

$$\Pi_{\pm} = \sum_0^{\infty} |\Psi_{n,\pm}\rangle \langle \Psi_{n,\pm}|, \quad \Pi_0 = |\Psi_0\rangle \langle \Psi_0|. \quad (35)$$

The projectors enable the interpretation of quasiprobability distributions  $P_{\pm} = P_{11} \pm P_{12i}/\cos\theta$  used for the description of the single-atom laser dynamics in the strong-field regime in a simple manner. One can show that

$$\langle 1|\Pi_{\pm}\rho\Pi_{\pm}|1\rangle \approx \frac{1}{2} \int d^2\alpha |\alpha\rangle \langle \alpha| P_{\pm}(\alpha) + O\left(\frac{1}{\langle n}\right). \quad (36)$$

Therefore, such combinations of quasiprobability distributions correspond to the dynamics of the system in subspaces of two types of states  $\{|\Psi_{n,+}\rangle\}_{n=1,2,\dots}$  and  $\{|\Psi_{n,-}\rangle\}_{n=1,2,\dots}$ , corresponding to the upper and lower Jaynes-Cummings ladders. At the same time, the evolution of field states, described by  $P_{\pm}$ , has a simple form and is reduced to the phase rotation of the coherent state.

If the average number of photons is sufficiently large, the state of the single-atom laser can be decomposed over the components, corresponding to the two subspaces, by neglecting the vacuum component  $\Pi_0|\Psi\rangle$ :

$$|\Psi\rangle \approx \Pi_+|\Psi\rangle + \Pi_-|\Psi\rangle. \quad (37)$$

Equation (34) implies that the evolution of components is described by the following expression (in the interaction representation):

$$\Pi_{\pm}|\Psi(t)\rangle = \exp(\pm i\kappa t \sqrt{\eta} a^\dagger a) \Pi_{\pm}|\Psi(0)\rangle + O\left(\frac{1}{\langle n}\right). \quad (38)$$

The solution can be sought in the form of a coherent state with a time-dependent amplitude

$$\Pi_{\pm}|\Psi(t)\rangle \sim \Pi_{\pm}|\alpha_{\pm}(t), 1\rangle, \quad (39)$$

where Eq. (38) implies (see Appendix G) that

$$\alpha_{\pm}(t) = e^{\pm i\kappa t \sqrt{\eta}/2\alpha_0} \alpha_0. \quad (40)$$

Therefore, the general state of the atom and the field has the form

$$|\Psi(t)\rangle = e^{i\kappa t \sqrt{\eta} \alpha_0/2} |\alpha_0 e^{i\kappa t \sqrt{\eta}/(2\alpha_0)}\rangle |+\rangle + e^{-i\kappa t \sqrt{\eta} \alpha_0/2} |\alpha_0 e^{-i\kappa t \sqrt{\eta}/(2\alpha_0)}\rangle |-\rangle + O\left(\frac{1}{\langle n}\right), \quad (41)$$

where the qubit states  $|\pm\rangle = (|1\rangle \pm |2\rangle)/\sqrt{2}$  are introduced.

Under the condition  $2\pi|\alpha_0| \gtrsim \kappa t \sqrt{\eta} \gg 1$ , the states  $|\alpha_0 e^{i\kappa t \sqrt{\eta}/(2\alpha_0)}\rangle$  and  $|\alpha_0 e^{-i\kappa t \sqrt{\eta}/(2\alpha_0)}\rangle$  become almost orthogonal and the expression (41) describes a state with hybrid atom-field entanglement, while the conditional states  $\rho_{11}$  and  $\rho_{22}$  are Schrödinger-cat states. The typical timescale of the nonclassicality buildup is  $\kappa t_f \sim 1/\sqrt{\eta}$ .

The incoherent transitions, caused by the interaction between the atom and the environment with the rates  $R_{12}$  and  $R_{21}$ , mix the subspaces determined by the projectors  $\Pi_+$  and  $\Pi_-$  and transform the superposition (41) into a mixed state. The typical timescale of the decay of the coherence-based nonclassicality is  $\kappa t_d \sim 1/(a_0^2 + \nu_0 + \frac{1}{2})$ .

Comparing Eqs. (31) and (41), we get the following relations for the parameters  $\xi$ ,  $\chi$ , and  $\varphi$  of the Schrödinger-cat state:

$$\chi/\xi \approx \tan \frac{\kappa t \sqrt{\eta}}{2\alpha_0}, \quad \varphi = \kappa t \sqrt{\eta} \alpha_0. \quad (42)$$

Dotted lines in Fig. 6 show the constructed estimates of the parameters, where the exponential decay of the coherent states amplitude  $|\alpha_{\pm}(t)| \approx \alpha_0 e^{-\kappa t}$  is also taken into account.

To check the presence of the predicted atom-field entanglement in the numerically simulated states, we analyze the von Neumann entropy  $S(\rho) = -\text{Tr}(\rho \log_2 \rho)$  of the whole system density operator  $\rho$  and of the reduced density operators  $\rho_{\text{field}} = \text{Tr}_{\text{atom}} \rho$  and  $\rho_{\text{atom}} = \text{Tr}_{\text{field}} \rho$  for the subsystems (the field mode and the atom, respectively). If the state  $\rho$  is separable, the entropy satisfies the inequalities  $S(\rho) \geq S(\rho_{\text{field}})$  and  $S(\rho) \geq S(\rho_{\text{atom}})$  [84,85]. Figure 7 shows that the latter inequality is violated for  $0.01 \lesssim \kappa t \lesssim 0.06$  (model 1) and  $0.01 \lesssim \kappa t \lesssim 0.12$  (model 2), indicating the presence of entanglement in the considered system.

### V. INCOHERENT STAGE

The dissipative processes (the incoherent pump and decay of the qubit, the dephasing, and the resonator loss) eventually erase the information about the phase of the initial coherent state of the field. Geometrically, this looks like closing the arc, which describes the angular distribution of quasiprobability, accompanied by the reduction of its diameter due to energy loss [Fig. 8(a)] taking place until the stationary state is reached.

Further, it is convenient to consider phase-averaged quasiprobability distributions, defined as

$$P_z(r) = \int_0^{2\pi} d\theta P_z(\alpha = r e^{i\theta}; s), \quad z = 11, 22, \text{Re}, \text{Im}. \quad (43)$$

Figures 8(b) and 8(c) show the evolution of such phase-averaged distributions for the two parameters sets, used for simulation of Fig. 1. The system state evolution, shown in Fig. 8(b) for model 2, is quite trivial: The most probable coherent state amplitude monotonically decreases until reaching the stationary value. The dynamics of model 1 in Fig. 8(c) is quite different. In the high-amplitude region B, the almost-exponential decay of the most probable coherent state amplitude occurs similarly to the previous case. However, there exists a certain border [the gap G in Fig. 8(c) and the dot-dashed circle in Fig. 9(a)] at which the quasiprobability distribution (instead of shrinking to the stationary state) takes a double-maximum shape and effectively tunnels to the region A of smaller amplitudes. Such peculiar behavior of the quasiprobability distributions closely resembles the amplitude bistability phenomenon [22,24] and photon-blockade breakdown bistability [12–14] reported for continuous coherent excitation of a single-atom laser. Also, similar amplitude bistability can emerge due to nonlinearity of the considered cavity [50]. However, in our case the effect is caused by the inherent nonlinearity of the single-emitter system rather than by external modification of its decay.

To get a better notion of the analogy between the discussed dynamics of the single-qubit laser with incoherent pumping

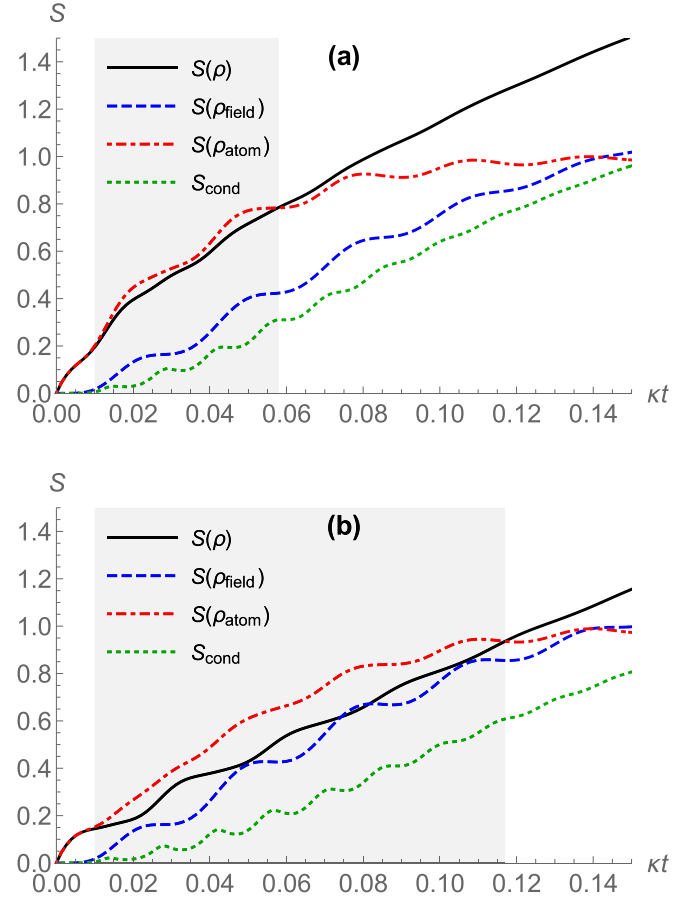


FIG. 7. von Neumann entropy of the whole system state  $\rho$  (solid black lines) and subsystems' reduced states  $\rho_{\text{field}}$  (blue dashed lines) and  $\rho_{\text{atom}}$  (red dot-dashed lines) for (a) model 1 and (b) model 2. In the shadowed regions, the state is entangled since the separability condition  $S(\rho) \geq S(\rho_{\text{atom}})$  is violated. The dotted green line shows the averaged conditional entropy of the field state  $S_{\text{cond}} = S(\rho_{11})\text{Tr}\rho_{11} + S(\rho_{22})\text{Tr}\rho_{22}$ , characterizing the mixedness of the field state if the qubit state is measured in the basis of the ground  $|1\rangle$  and excited  $|2\rangle$  states. For  $\kappa t \lesssim 0.08$  the conditional states possess relatively low entropy. The results are obtained by numerical solution of Eqs. (4)–(6) in the Fock-state representation for a truncated subspace with the number of photons  $n \leq 140$ .

and initial coherent excitation with the amplitude bistability, it is useful to consider the expression (A3) from Ref. [22], which provides the semiclassical steady-state solution

$$\frac{E}{\kappa} = \langle \bar{a} \rangle \left( 1 + 2 \frac{\eta}{v + 8\langle \bar{a} \rangle \eta / v} \right), \quad (44)$$

where  $E$  is the strength of coherent pumping,  $\langle \bar{a} \rangle$  is the semiclassical steady-state field amplitude, and the notation  $v = \gamma/\kappa$  is introduced for the normalized rate of the qubit-environment interaction  $\gamma$  used in Ref. [22]. Following the idea of Eq. (23), one can formally establish the correspondence  $E(t) \sim \kappa \alpha_0 e^{-\kappa t}$  indicating the analogy between continuous coherent pumping and the decaying effect of initial (pulsed) coherent excitation. Since for  $\eta \gg 1$  the effects caused by the coherent qubit-field interaction are much faster than the decay of the initial coherent state amplitude decay

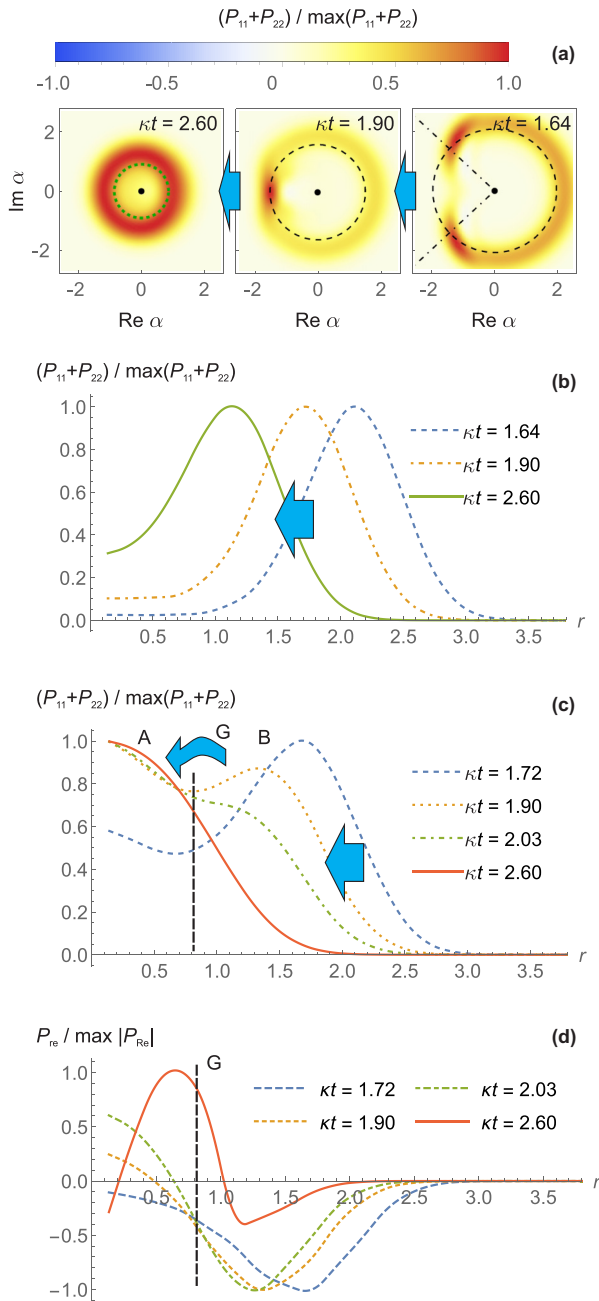


FIG. 8. Incoherent stage of the single-qubit laser dynamics. (a) Quasiprobability distribution  $P_{11}(\alpha; s) + P_{22}(\alpha; s)$  for model 2. The dashed circle corresponds to the exponential decay of the field amplitude  $\alpha_0 e^{-\kappa t}$ . The dotted green circle shows the most probable amplitude for the stationary state, approached for  $\kappa t \gtrsim 5$ . The dot-dashed line indicates the angular directions, calculated according to Eq. (22). (b) Phase-averaged quasiprobability distribution  $P_{11}(r) + P_{22}(r)$  for the same simulation parameters. The maximum of the distribution moves in the direction shown by the arrow until reaching the stationary state. (c) Phase-averaged quasiprobability distribution  $P_{11}(r) + P_{22}(r)$  for model 1 [the simulation parameters from Fig. 1(a)]. The maximum of the distribution moves in the direction shown by the straight arrow until reaching region B. Then the distribution tunnels over the gap G to region A, containing the stationary quasiprobability distribution. (d) Phase-averaged quasiprobability distribution  $P_{\text{re}}(r)$  for the same simulation parameters (model 1).

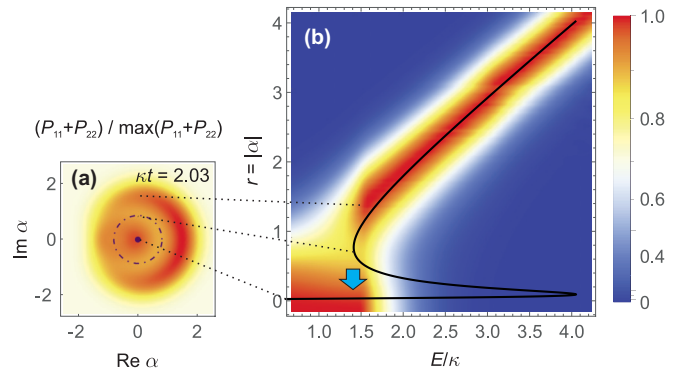


FIG. 9. Analogy with amplitude bistability. (a) Quasiprobability distribution  $P_{11}(\alpha; s) + P_{22}(\alpha; s)$  for model 1. The dot-dashed circle indicates the gap between the two maxima of quasiprobability denoted by G in Fig. 8. (b) Evolution of the phase-averaged quasiprobability distribution  $P_{11}(r) + P_{22}(r)$  expressed in terms of the effective pump strength for the same simulation parameters. For each  $E/\kappa$ , the shown quasiprobabilities are normalized by the maximal value. The overlain black line shows the semiclassical solution according to Eq. (44). The gap in (a) corresponds to the tunneling between the upper and lower branches of the stable state curve.

$\alpha_0 \mapsto \alpha_0 e^{-\kappa t}$ , the semiclassical steady-state amplitude ( $\bar{\alpha}$ ) can be associated with the most probable coherent state amplitude according to the simulated quasiprobability distributions. The results of overlaying the semiclassical solution on the numerical simulation results are shown in Fig. 9(b). The optimal fit of the simulated data by the theoretical curve is achieved when the normalized rate of the qubit-environment interaction is chosen as  $\nu = (R_{21} - R_{12})/\kappa$ . Since the considered model corresponds to gradual decay of the effective coherent excitation, the downward curve of the bistability-induced hysteresis is engaged. The opposite upward trajectory with lower field amplitudes requires an adiabatic increase of the coherent excitation, which goes beyond the model analyzed here.

Additional insight into the reason for the tunneling of the quasiprobability distribution through the gap can be acquired from the analogy with the emergence of a bimodal distribution for photon-blockade breakdown [12,13]. There the effect is caused by switching between the two Jaynes-Cummings ladders of atom-field states, which correspond to the projectors  $\Pi_+$  and  $\Pi_-$  from Eq. (35), evolve almost independently, and are coupled by dissipation-induced jumps. The plot shown in Fig. 8(d) indicates similar separation of the states at two sides of the gap in the considered model of an incoherently pumped single-qubit laser. In the higher-amplitude region [to the right of the gap G in Figs. 8(c) and 8(d)] the quasiprobability distribution  $P_{\text{re}}$  takes negative values and indicates that the state belongs to the lower ladder (the subspace defined by the projector  $\Pi_-$ ). Similarly, the lower-amplitude region is characterized by positive values of  $P_{\text{re}}$  and corresponds to the upper ladder (defined by the projector  $\Pi_+$ ). The unitary atom-field coupling does not mix the two subspaces and the transition is caused by incoherent effects only, thus preserving the bimodal shape of the quasiprobability distributions for a considerable time.

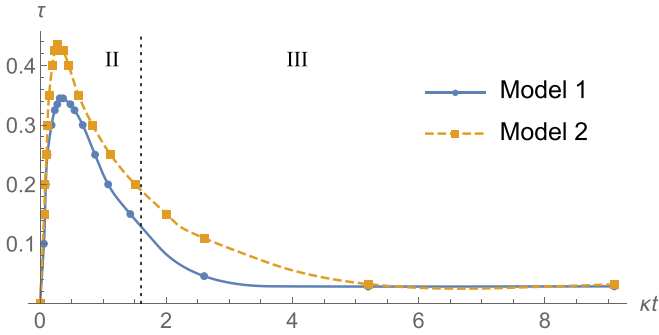


FIG. 10. Evolution of nonclassicality depth  $\tau$  of the field state  $\rho_{11} + \rho_{22}$  averaged over the qubit for model 1 (blue solid line) and model 2 (orange dashed line). The vertical dotted line schematically divides the coherent stage II and incoherent stage III of the dynamics.

The established analogy between the dynamics of the considered system and the amplitude bistability is quite formal and deserves a more detailed treatment, which goes beyond of the scope of the present work, which is mainly devoted to the nonclassicality of the generated states. However, the results in Figs. 8(d) and 9 clearly show that the discussed phenomena are closely connected to each other.

## VI. NONCLASSICALITY DYNAMICS

Figure 10 shows the dynamics of the nonclassicality depth. To obtain the shown curves, the evolution of the quasiprobability distributions is simulated for a set of ordering parameter values  $s$ . For each simulation result, the values  $\kappa t_1(s)$  and  $\kappa t_2(s)$ , such that the quasiprobability distribution  $P_{11}(\alpha; s) + P_{22}(\alpha; s)$  identifies the state nonclassicality (takes negative values) for  $\kappa t_1(s) < \kappa t < \kappa t_2(s)$ , are found and are plotted in Fig. 10. While the nonclassicality depth should be used with caution for a comparison of different classes of nonclassical states [77], we find that it provides an efficient and sensitive mathematical tool for quantitative nonclassicality analysis at different evolution stages of the same state.

The initial growth of the state nonclassicality is caused by the coherent qubit-field interaction and formation of a hybrid entangled Schrödinger-cat state at a timescale  $t_f$ . The resulting nonclassicality is limited by the incoherent interaction of the considered system with the environment, destroying quantum interference at  $t \sim t_d$ . For model 2, the lower decay rate of the qubit's excited state leads to longer preservation of quantum coherence and a larger maximal value of the nonclassicality depth.

While extracting the generated nonclassical state from the resonator may be challenging, there exist a number of fast unlock approaches applicable to optical [86–91] and microwave cavities [92]. Therefore, we expect that the generated states can indeed be useful for various metrology and quantum information processing tasks.

In particular, the Schrödinger-cat-like states, generated in the initial stages of the dynamics, can be useful for detection of small coherent displacements [93], described by the coherent displacement operator  $D(\varepsilon) = e^{\varepsilon(a^\dagger - a)} = e^{-2i\varepsilon Y}$ . The sensitivity of the state to the displacement parameter  $\varepsilon$  can be quantified by quantum Fisher information  $F_Q$  [94], which is

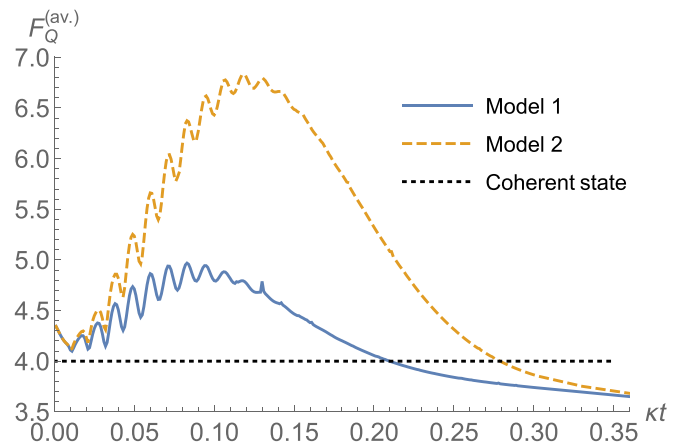


FIG. 11. Averaged quantum Fisher information for conditional field states for the dynamics of model 1 (blue solid line) and model 2 (orange dashed line). For comparison, the quantum Fisher information for a coherent state is shown by a black dotted line. The results are obtained by numerical solution of Eqs. (4)–(6) in the Fock-state representation for a truncated subspace with the number of photons  $n \leq 140$ .

equal to 4 for a coherent state and to

$$F_Q = 4 + \frac{16\chi^2}{1 + e^{-2\chi^2} \cos(2\xi\chi - \varphi)} \geq 4 \quad (45)$$

for a Schrödinger-cat state (31). Figure 11 shows the dependence of the averaged quantum Fisher information of conditional field states on the dimensionless state evolution time  $\kappa t$ . The displayed quantity is defined as  $F_Q^{(av.)} = F_Q(\rho_{11})\text{Tr}\rho_{11} + F_Q(\rho_{22})\text{Tr}\rho_{22}$ . For  $\kappa t \leq 0.21$  (model 1) and  $\kappa t \leq 0.28$  (model 2) the generated states provide better sensitivity to the analyzed displacement  $\varepsilon$  relative to coherent states. Similarly to the nonclassicality depth, the quantum advantages of the generated state survive longer for model 2 due to the lower decay rate of the qubit's excited state.

## VII. CONCLUSION

Our analysis of quasiprobability distributions for a single-qubit single-mode laser confirmed its efficiency and fruitfulness for gaining a better understanding of the dynamics of that fundamental model system. It enabled splitting the evolution of the incoherently pumped single-qubit laser with the initial (pulsed) coherent excitation of the field mode into two stages: one coherent and the other incoherent. While direct analysis of the system's density operator can conceal the differences between the stages, visualization of quasiprobabilities helps us distinguish them clearly.

We have shown that the dynamics of the incoherently pumped single-qubit laser reproduces the effects of phase and amplitude bistability, previously reported for systems with coherent driving. At intermediate stages of the system evolution, a strongly nonclassical state is generated. It possesses hybrid entanglement between the qubit and the field mode and can be mapped onto a field-only Schrödinger-cat state by measuring

the state of the qubit. Such a state can be useful, for example, for encoding quantum information or for quantum metrology.

Also, analysis of quasiprobability distributions was shown to be useful for quantification of the generated state nonclassicality and determination of the optimal conditions for nonclassical state generation.

#### APPENDIX A: REGULARITY OF QUASIPROBABILITY DISTRIBUTIONS IN THE STATIONARY STATE

The stationary field state of an incoherently pumped single-qubit laser is diagonal in the Fock-state basis [33] and has the asymptotics  $\rho_{nn} \sim (\eta a_0)^{2n}/(n!)^2$ . Each Fock state  $|n\rangle$  maps onto the quasiprobability distribution [72]

$$P_n(\alpha; s) = \frac{2}{1-s} \left( -\frac{1+s}{1-s} \right)^n \exp\left( -\frac{2|\alpha|^2}{1-s} \right) \times L_n\left( \frac{4|\alpha|^2}{1-s^2} \right). \quad (\text{A1})$$

The Laguerre polynomial has the representation

$$L_n(x) = \sum_{k=0}^n \binom{n}{k} \frac{(-x)^k}{k!}, \quad (\text{A2})$$

which implies  $|L_n(x)| < (1+|x|)^n$ .

The  $s$ -ordered quasiprobability distribution can be expressed in the following form for the stationary state:

$$P(\alpha; s) = \sum_{n=0}^{\infty} \rho_{nn} P_n(\alpha; s). \quad (\text{A3})$$

Here each term is bounded according to

$$|\rho_{nn} P_n(\alpha; s)| < \frac{\text{const}}{(n!)^2} \left[ \eta^2 a_0^2 \frac{1+s}{1-s} \left( 1 + \frac{4|\alpha|^2}{1-s^2} \right) \right]^n \times \exp\left( -\frac{2|\alpha|^2}{1-s} \right) \quad (\text{A4})$$

and convergence of the sum is ensured for any  $\alpha$  and  $s < 1$ .

#### APPENDIX B: EXPRESSIONS FOR CONVECTION AND ABSORPTION COEFFICIENTS

Here the expressions for the coefficients in Eq. (14) are given. The absorption coefficient  $a$  is described by the following matrix:

$$a = \begin{pmatrix} 4a_0^2 & -(4\nu_0 + 2) & -2\sqrt{\eta}x & 2\sqrt{\eta}y \\ -4a_0^2 & 4\nu_0 + 2 & 2\sqrt{\eta}x & -2\sqrt{\eta}y \\ \sqrt{\eta}x & -\sqrt{\eta}x & 2\mu_0 + 1 & 0 \\ -\sqrt{\eta}y & \sqrt{\eta}y & 0 & 2\mu_0 + 1 \end{pmatrix}. \quad (\text{B1})$$

The convection coefficient  $\beta$  is a  $4 \times 4$  matrix, where each element is a two-component vector mapped to a scalar

differential operator after multiplication by  $\nabla$ ,

$$\beta \cdot \nabla = \begin{pmatrix} 0 & 0 & 2D_x^{(+)} & -2D_y^{(+)} \\ 0 & 0 & 2D_x^{(-)} & -2D_y^{(-)} \\ D_x^{(-)} & D_x^{(+)} & 0 & 0 \\ -D_y^{(-)} & -D_y^{(+)} & 0 & 0 \end{pmatrix}, \quad (\text{B2})$$

where

$$D_x^{(\pm)} = \frac{\sqrt{\eta}(1 \pm s)}{4} \frac{\partial}{\partial x}, \quad D_y^{(\pm)} = \frac{\sqrt{\eta}(1 \pm s)}{4} \frac{\partial}{\partial y}. \quad (\text{B3})$$

#### APPENDIX C: OPTIMAL ORDERING PARAMETER VALUE FOR VISUALIZATION OF QUASIPROBABILITY DISTRIBUTIONS

Figure 12 shows the single-qubit laser dynamics for different values of the ordering parameter  $s$ , describing smoothness of the quasiprobability distributions. The optimal value of  $s$  should ensure demonstration of all the discussed stages of dynamics and regions of the phase space, sufficient sensitivity to the generated state nonclassicality, and stability and fast convergence of numerical calculations.

According to the definition of the nonclassicality depth  $\tau$ , the quasiprobability distributions for  $s \leq s_{\min} = 1 - 2\tau_{\max}$ , where  $\tau_{\max}$  is the maximal value of the nonclassicality depth achieved during the dynamics, are not suitable for detection of the field-state nonclassicality. In particular, the critical value is  $s_{\min} = 0.31$  for model 1 (Fig. 10) and the quasiprobability distribution, shown in Fig. 12(d) for  $s = 0.2$ , remains positive during all stages of dynamics. The distribution in Fig. 12(c) corresponds to  $s$  slightly larger than  $s_{\min}$  and indicates generation of a nonclassical state at the beginning of the coherent stage II. However, during the remaining part of the coherent stage of dynamics, the interference region is suppressed because of too strong smoothing of the quasiprobability distribution.

The quasiprobability distribution for  $s = 0.65$ , shown in Fig. 12(a), demonstrates the opposite behavior. The interference region is characterized by fast high-amplitude oscillations, which obscure the arc in the image and may lead to numerical instability if the calculation mesh is not fine enough.

The optimal trade-off between the sensitivity to the state nonclassicality and numerical stability (for particular values of the model parameters) is achieved for  $s \approx 0.5$ . That value is used for simulation of the data shown in Figs. 1,2,4–6,8,9.

#### APPENDIX D: APPROXIMATE EQUATIONS FOR THE ARC REGION

The characteristic scales of the arc region, which can be noticed from the numerical modeling results, are  $P_z(\alpha; s)$ ,  $\partial P_z/\partial x$ , and  $\partial P_z/\partial y = O(1)$ , with  $(1/\kappa)\partial P_z/\partial t = O(r)$ , where  $z = 11, 22, \text{Re}, \text{Im}$ . Therefore, the terms on the right-hand side of Eq. (14) have the orders  $c\Delta u = O(1)$ ,  $\nabla \cdot (\gamma u) = O(r)$ ,  $(\beta \cdot \nabla)u = O(\sqrt{\eta})$ , and  $au = O(r\sqrt{\eta})$ . For  $\eta \gg 1$ , the leading order of decomposing Eq. (14) reads

$$O(r) = O(r) + O(\sqrt{\eta}) + \sqrt{\eta}r\tilde{a}u, \quad (\text{D1})$$

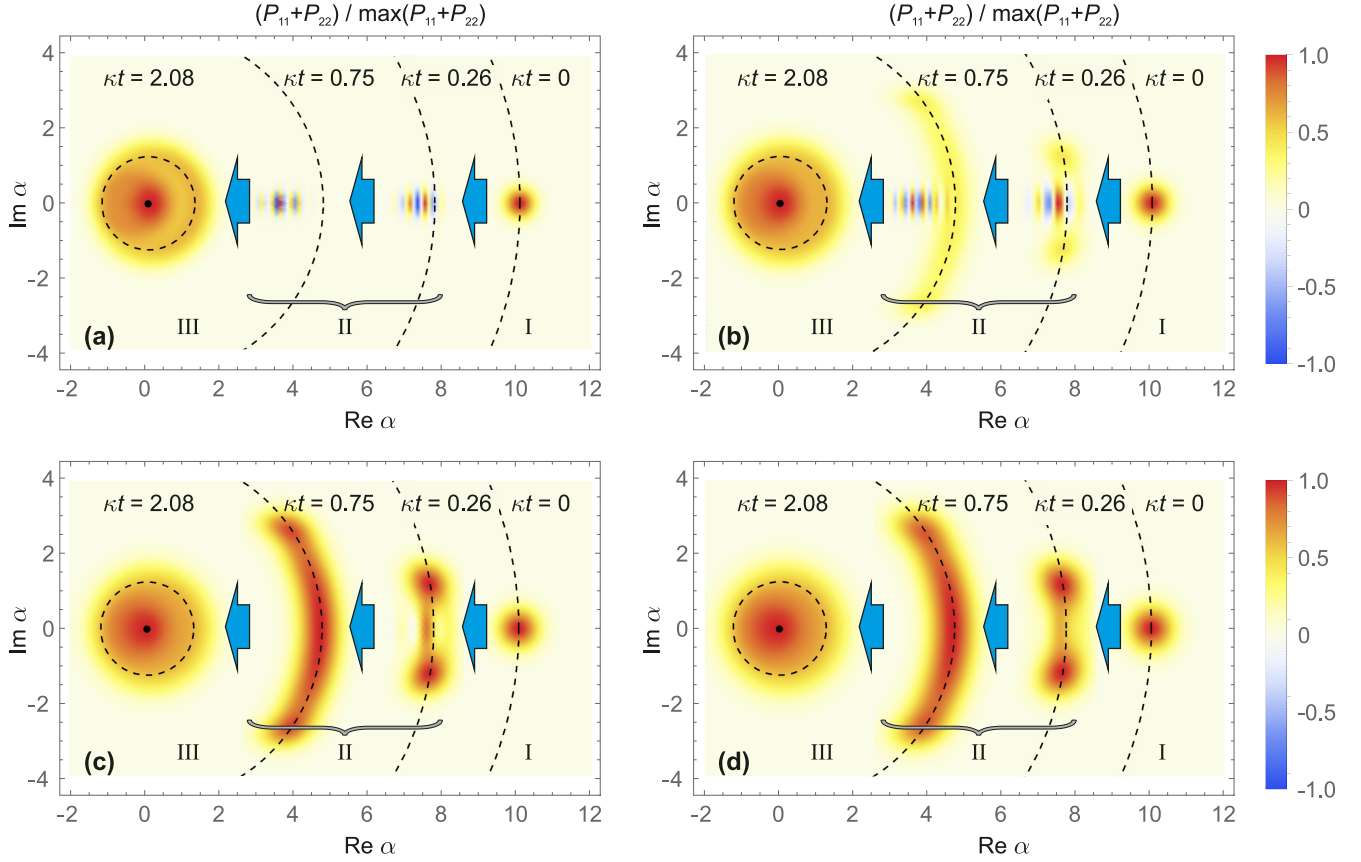


FIG. 12. Overlain quasiprobability distributions  $P_{11}(\alpha; s) + P_{22}(\alpha; s)$  for different stages of the single-qubit laser dynamics and different values of the ordering parameter  $s$ : (a) 0.65, (b) 0.50, (c) 0.35, and (d) 0.20. The notation of the stages, the meaning of dashed lines, and the parameters of the model are the same as in Fig. 1(a). The quasiprobability distributions are normalized by their maximal values.

where

$$\tilde{a} = \begin{pmatrix} 0 & 0 & -2 \cos \theta & 2 \sin \theta \\ 0 & 0 & 2 \cos \theta & -2 \sin \theta \\ \cos \theta & -\cos \theta & 0 & 0 \\ -\sin \theta & \sin \theta & 0 & 0 \end{pmatrix} \quad (\text{D2})$$

is the part of matrix  $a$ , proportional to  $\sqrt{\eta}r$ .

The matrix  $\tilde{a}$  has two zero eigenvalues, corresponding to the combinations  $(P_{11} + P_{22})/2$  and  $P_{\text{Re}} \sin \theta + P_{\text{Im}} \cos \theta$ . Those combinations are not constrained by Eq. (D1). The two remaining (orthogonal) combinations must be small enough to satisfy Eq. (D1) as indicated by Eq. (18). Therefore, one can reduce the set of considered quasiprobability distributions to

$$\frac{P_{11} + P_{22}}{2} \approx P_{11} \quad (\text{D3})$$

and

$$P_{\text{Re}} \sin \theta + P_{\text{Im}} \cos \theta \approx \frac{P_{\text{Im}}}{\cos \theta}. \quad (\text{D4})$$

The reduced two-component quasiprobability vector  $u' = (P_{11}(\alpha; s), P_{\text{Im}}(\alpha; s)/\cos \theta)^T$  satisfies the partial differential equation

$$i\dot{u}' = c\Delta u' + \nabla \cdot (\gamma u') - (\beta' \cdot \nabla)u' - a'u' + O\left(\frac{1}{r}, \frac{1}{\sqrt{\eta}}\right), \quad (\text{D5})$$

where

$$(\beta' \cdot \nabla) = -\frac{\sqrt{\eta}}{2r} \begin{pmatrix} 0 & 1 \\ 1 & 0 \end{pmatrix} \frac{\partial}{\partial \theta} \quad (\text{D6})$$

and

$$a' = \begin{pmatrix} 0 & 0 \\ 0 & 2\mu_0 + 1 \end{pmatrix}. \quad (\text{D7})$$

Further, the matrix in Eq. (D6) can be diagonalized by rotation of the vector  $u'$  induced by introduction of the linear combinations of the quasiprobability distributions according to Eq. (19). Then Eq. (D5) takes the form (20).

#### APPENDIX E: APPROXIMATE EXPRESSIONS FOR THE INTERFERENCE REGION

The characteristic scales of the interference region are  $P_z(\alpha; s)$ ,  $\partial P_z/\partial y = O(1)$ ,  $(1/\kappa)\partial P_z/\partial t = O(r)$ , and  $\partial P_z/\partial x = O(\sqrt{\eta})$ , where  $z = 11, 22$ , Re, Im. The leading order of decomposing Eq. (14) is  $O(\eta, \sqrt{\eta}x)$  and yields Eqs. (25)–(28). Their solution in the form (29) can be found for the parameters  $k$  and  $\omega$  obeying Eq. (30) and the relative amplitudes and phases being connected by the relations

$$b_{11,22} = \frac{2\sqrt{\eta}}{k} \frac{s}{1-s} \sqrt{\frac{k^2(1 \pm s)^2 + 16}{k^2 s^2 + 16}} \quad (\text{E1})$$

and

$$\tan(\varphi_{11,22} - \varphi_{\text{Re}}) = -\left[\frac{ks(1-s)}{4x} \pm \frac{4x}{k}\right], \quad (\text{E2})$$

where the signs + and - correspond to indices 11 and 22, respectively.

#### APPENDIX F: FITTING THE GENERATED STATE BY A SCHRÖDINGER CAT STATE

To fit a certain field state  $\rho$  (e.g., the conditional state  $\rho_{11}$ ) by a Schrödinger-cat state (31), it is useful to relate the parameters  $\xi$  and  $\chi$  of the state to moments of the field quadratures  $X = (a + a^\dagger)/2$  and  $Y = (a - a^\dagger)/2i$ . Direct calculations show that the following relations hold for the state (31):

$$\langle X \rangle = \xi - \frac{\chi e^{-2\chi^2} \sin \phi}{1 + e^{-2\chi^2} \cos \phi}, \quad (\text{F1})$$

$$\Delta Y^2 = \langle Y^2 \rangle - \langle Y \rangle^2 = \frac{1}{4} + \frac{\chi^2}{1 + e^{-2\chi^2} \cos \phi}. \quad (\text{F2})$$

Here the parameter  $\phi = 2\xi\chi - \varphi$  is introduced. On the other hand, the values  $\langle X \rangle$  and  $\Delta Y^2$  can be calculated from the quasiprobability distribution  $P(\alpha; s)$ , describing the considered state  $\rho$ , in the following way:

$$\langle X \rangle = \bar{X}, \quad \Delta Y^2 = \frac{1}{4} + \frac{1-s}{4} + (\bar{Y}^2 - \bar{Y}^2). \quad (\text{F3})$$

Here the notation  $\overline{f(a, a^\dagger)}$  corresponds to averaging over the quasiprobability distribution:

$$\overline{f(a, a^\dagger)} = \int d^2\alpha P(\alpha; s) f(\alpha, \alpha^*). \quad (\text{F4})$$

For a given value of  $\phi$ , the parameters  $\xi$  and  $\chi$  can be found from Eqs. (F1) and (F2). To estimate the parameter  $\phi$  itself, the quasiprobability distribution  $P(\alpha; s)$  can be fitted by the expression (32). Since the right-hand sides of Eqs. (F1) and (F2) have a weak dependence of  $\phi$ , the procedure can be performed iteratively, where each iteration includes fitting of  $\phi$  for fixed  $\xi$  and  $\chi$  and subsequent update of  $\xi$  and  $\chi$  for the found  $\phi$ .

#### APPENDIX G: PHASE ROTATION OF A COHERENT STATE

To derive Eq. (40) from Eqs. (38) and (39), one needs to describe the action of the operator having the form  $\exp(i\xi\sqrt{a^\dagger}a)$  at a coherent state  $|\alpha\rangle$  with a large amplitude  $|\alpha| \gg 1$ . The calculations can be performed by explicitly using the coherent displacement operator  $D(\alpha) = \exp(\alpha a^\dagger - \alpha^* a)$ :

$$\begin{aligned} e^{i\xi\sqrt{a^\dagger}a}|\alpha\rangle &= D(\alpha)D^\dagger(\alpha)e^{i\xi\sqrt{a^\dagger}a}D(\alpha)|0\rangle \\ &= D(\alpha)e^{i\xi\sqrt{(a^\dagger+\alpha^*)(a+\alpha)}}|0\rangle \\ &\approx e^{i\xi|\alpha|}D(\alpha)\exp\left[i\xi\frac{\alpha}{2|\alpha|}a^\dagger - \left(i\xi\frac{\alpha}{2|\alpha|}\right)^*a\right]|0\rangle \\ &\approx e^{i\xi|\alpha|/2}D(\alpha e^{i\xi/2|\alpha|})|0\rangle = e^{i\xi|\alpha|/2}|\alpha e^{i\xi/2|\alpha|}\rangle. \end{aligned} \quad (\text{G1})$$

The error of the approximation used has the order of magnitude  $O(1/|\alpha|)$ .

- 
- [1] R. J. Thompson, G. Rempe, and H. J. Kimble, Observation of Normal-Mode Splitting for an Atom in an optical Cavity, *Phys. Rev. Lett.* **68**, 1132 (1992).
- [2] A. Boca, R. Miller, K. M. Birnbaum, A. D. Boozer, J. McKeever, and H. J. Kimble, Observation of the Vacuum Rabi Spectrum for One Trapped Atom, *Phys. Rev. Lett.* **93**, 233603 (2004).
- [3] O. Astafiev, A. M. Zagoskin, A. A. Abdumalikov, Y. A. Pashkin, T. Yamamoto, K. Inomata, Y. Nakamura, and J. S. Tsai, Resonance fluorescence of a single artificial atom, *Science* **327**, 840 (2010).
- [4] Y. Kaluzny, P. Goy, M. Gross, J. M. Raimond, and S. Haroche, Observation of Self-Induced Rabi Oscillations in Two-Level Atoms Excited Inside a Resonant Cavity: The Ringing Regime of Superradiance, *Phys. Rev. Lett.* **51**, 1175 (1983).
- [5] T. Yoshie, A. Scherer, J. Hendrickson, G. Khitrova, H. M. Gibbs, G. Rupper, C. Ell, O. B. Shchekin, and D. G. Deppe, Vacuum Rabi splitting with a single quantum dot in a photonic crystal nanocavity, *Nature (London)* **432**, 200 (2004).
- [6] J. H. Eberly, N. B. Narozhny, and J. J. Sanchez-Mondragon, Periodic Spontaneous Collapse and Revival in a Simple Quantum Model, *Phys. Rev. Lett.* **44**, 1323 (1980).
- [7] G. Rempe, H. Walther, and N. Klein, Observation of Quantum Collapse and Revival in a One-Atom Maser, *Phys. Rev. Lett.* **58**, 353 (1987).
- [8] L. Tian and H. J. Carmichael, Quantum trajectory simulations of two-state behavior in an optical cavity containing one atom, *Phys. Rev. A* **46**, R6801 (1992).
- [9] A. Imamoğlu, H. Schmidt, G. Woods, and M. Deutsch, Strongly Interacting Photons in a Nonlinear Cavity, *Phys. Rev. Lett.* **79**, 1467 (1997).
- [10] K. M. Birnbaum, A. Boca, R. Miller, A. D. Boozer, T. E. Northup, and H. J. Kimble, Photon blockade in an optical cavity with one trapped atom, *Nature (London)* **436**, 87 (2005).
- [11] C. Lang, D. Bozyigit, C. Eichler, L. Steffen, J. M. Fink, A. A. Abdumalikov, Jr. M. Baur, S. Filipp, M. P. da Silva, A. Blais, and A. Wallraff, Observation of Resonant Photon Blockade at Microwave Frequencies Using Correlation Function Measurements, *Phys. Rev. Lett.* **106**, 243601 (2011).
- [12] H. J. Carmichael, in *Proceedings of the Rochester Conferences on Coherence and Quantum Optics and the Quantum Information and Measurement Meeting* (Optica Publishing Group, Washington, DC, 2013), paper W2B.3.

- [13] H. J. Carmichael, Breakdown of Photon Blockade: A Dissipative Quantum Phase Transition in Zero Dimensions, *Phys. Rev. X* **5**, 031028 (2015).
- [14] J. M. Fink, A. Dombi, A. Vukics, A. Wallraff, and P. Domokos, Observation of the Photon-Blockade Breakdown Phase Transition, *Phys. Rev. X* **7**, 011012 (2017).
- [15] J. McKeever, A. Boca, A. D. Boozer, J. R. Buck, and H. J. Kimble, Experimental realization of a one-atom laser in the regime of strong coupling, *Nature (London)* **425**, 268 (2003).
- [16] K. Hennessy, A. Badolato, M. Winger, D. Gerace, M. Atatüre, S. Gulde, S. Fält, E. L. Hu, and A. Imamoglu, Quantum nature of a strongly coupled single quantum dot-cavity system, *Nature (London)* **445**, 896 (2007).
- [17] G. M. Meyer, M. Löffler, and H. Walther, Spectrum of the ion-trap laser, *Phys. Rev. A* **56**, R1099 (1997).
- [18] A. D. Boozer, Laserlike and atomlike regimes in a one-atom laser, *Phys. Rev. A* **78**, 053814 (2008).
- [19] F. Dubin, C. Russo, H. G. Barros, A. Stute, C. Becher, P. O. Schmidt, and R. Blatt, Quantum to classical transition in a single-ion laser, *Nat. Phys.* **6**, 350 (2010).
- [20] N. V. Larionov, K. A. Barantsev, and E. N. Popov, Single-atom laser with a low-finesse cavity operating in the strong-coupling regime, *St. Petersburg Polytech. Univ. J. - Phys. Math.* **11**, 99 (2018).
- [21] X. Guo, S. Lü, and Z. Ren, Coherence and statistics of a one-atom laser in a photonic crystal microcavity, *J. Phys. B* **43**, 225401 (2010).
- [22] S. Y. Kilin and T. B. Krinitskaya, Single-atom phase bistability in a fundamental model of quantum optics, *J. Opt. Soc. Am. B* **8**, 2289 (1991).
- [23] M. A. Armen, A. E. Miller, and H. Mabuchi, Spontaneous Dressed-State Polarization in the Strong Driving Regime of Cavity QED, *Phys. Rev. Lett.* **103**, 173601 (2009).
- [24] J. Kerckhoff, M. A. Armen, and H. Mabuchi, Remnants of semiclassical bistability in the few-photon regime of cavity QED, *Opt. Express* **19**, 24468 (2011).
- [25] M. Mantovani, A. D. Armour, W. Belzig, and G. Rastelli, Dynamical multistability in a quantum-dot laser, *Phys. Rev. B* **99**, 045442 (2019).
- [26] P. Filipowicz, J. Javanainen, and P. Meystre, Theory of a microscopic maser, *Phys. Rev. A* **34**, 3077 (1986).
- [27] S. Y. Kilin and T. B. Karlovich, Single-atom laser: Coherent and nonclassical effects in the regime of a strong atom-field correlation, *J. Exp. Theor. Phys.* **95**, 805 (2002).
- [28] J. McKeever, A. Boca, A. D. Boozer, R. Miller, J. R. Buck, A. Kuzmich, and H. J. Kimble, Deterministic generation of single photons from one atom trapped in a cavity, *Science* **303**, 1992 (2004).
- [29] T. Wilk, S. C. Webster, A. Kuhn, and G. Rempe, Single-atom single-photon quantum interface, *Science* **317**, 488 (2007).
- [30] J. Simon, H. Tanji, J. K. Thompson, and V. Vuletić, Interfacing Collective Atomic Excitations and Single Photons, *Phys. Rev. Lett.* **98**, 183601 (2007).
- [31] W. Choi, J.-H. Lee, K. An, C. Fang-Yen, R. R. Dasari, and M. S. Feld, Observation of Sub-Poisson Photon Statistics in the Cavity-QED Microlaser, *Phys. Rev. Lett.* **96**, 093603 (2006).
- [32] P. Lougovski, F. Casagrande, A. Lulli, and E. Solano, Strongly driven one-atom laser and decoherence monitoring, *Phys. Rev. A* **76**, 033802 (2007).
- [33] S. Y. Kilin and A. B. Mikhalychev, Single-atom laser generates nonlinear coherent states, *Phys. Rev. A* **85**, 063817 (2012).
- [34] S. Y. Kilin and A. B. Mikhalychev, Nonlinearity and nonclassicality in single-qubit laser operation, *Phys. Scr.* **2014**, 014021 (2014).
- [35] V. P. Stefanov and S. Y. Kilin, Squeezed states engineering by coherent pulses train acting on single atom laser, *Nonlinear Phenom. Complex Syst.* **22**, 64 (2019).
- [36] V. A. Bobrikova, R. A. Khachatryan, K. A. Barantsev, and E. N. Popov, Quantum squeezing of the field of a single-atom laser under conditions of a variable coupling constant, *Opt. Spectrosc.* **127**, 1070 (2019).
- [37] C. J. Villas-Boas, K. N. Tolazzi, B. Wang, C. Ianzano, and G. Rempe, Continuous Generation of Quantum Light from a Single Ground-State Atom in an Optical Cavity, *Phys. Rev. Lett.* **124**, 093603 (2020).
- [38] D. B. Horoshko, C.-S. Yu, and S. Y. Kilin, Time-ordering effects in a one-atom laser based on electromagnetically induced transparency, *J. Opt. Soc. Am. B* **38**, 3088 (2021).
- [39] M. Kiffner, M. S. Zubairy, J. Evers, and C. H. Keitel, Two-mode single-atom laser as a source of entangled light, *Phys. Rev. A* **75**, 033816 (2007).
- [40] X.-Y. Lü, J.-B. Liu, L.-G. Si, and X. Yang, Continuous-variable entanglement in a two-mode four-level single-atom laser, *J. Phys. B* **41**, 035501 (2008).
- [41] Q. X. Mu, Y. H. Ma, and L. Zhou, Entanglement generation in a two-mode single-atom laser, *Eur. Phys. J. D* **51**, 375 (2009).
- [42] X. Hao, X.-Y. Lü, L. Liu, and X. Yang, Continuous-variable entanglement via an incoherent pump in a microwave-driven  $\Lambda$ -type single-atom laser, *J. Phys. B* **42**, 105502 (2009).
- [43] E. A. Sete and C. H. R. Ooi, Continuous-variable entanglement and two-mode squeezing in a single-atom Raman laser, *Phys. Rev. A* **85**, 063819 (2012).
- [44] G. M. Meyer, H.-J. Briegel, and H. Walther, Ion-trap laser, *Europhys. Lett.* **37**, 317 (1997).
- [45] B. Jones, S. Ghose, J. P. Clemens, P. R. Rice, and L. M. Pedrotti, Photon statistics of a single atom laser, *Phys. Rev. A* **60**, 3267 (1999).
- [46] H.-J. Kim, A. H. Khosa, H.-W. Lee, and M. S. Zubairy, One-atom correlated-emission laser, *Phys. Rev. A* **77**, 023817 (2008).
- [47] L. Florescu, S. John, T. Quang, and R. Wang, Theory of a one-atom laser in a photonic band-gap microchip, *Phys. Rev. A* **69**, 013816 (2004).
- [48] L. Florescu, Nonclassical light generation by a photonic-crystal one-atom laser, *Phys. Rev. A* **78**, 023827 (2008).
- [49] R. Tan, G.-X. Li, and Z. Ficek, Squeezed single-atom laser in a photonic crystal, *Phys. Rev. A* **78**, 023833 (2008).
- [50] X.-Y. Guo and S.-C. Lü, Controllable optical bistability in photonic-crystal one-atom laser, *Phys. Rev. A* **80**, 043826 (2009).
- [51] C. M. Savage, Stationary Two-Level Atomic Inversion in a Quantized Cavity Field, *Phys. Rev. Lett.* **60**, 1828 (1988).
- [52] Y. Mu and C. M. Savage, One-atom lasers, *Phys. Rev. A* **46**, 5944 (1992).
- [53] C. Ginzl, H.-J. Briegel, U. Martini, B.-G. Englert, and A. Schenzle, Quantum optical master equations: The one-atom laser, *Phys. Rev. A* **48**, 732 (1993).
- [54] D. A. Rodrigues, J. Imbers, and A. D. Armour, Quantum Dynamics of a Resonator Driven by a Superconducting Single-

- Electron Transistor: A Solid-State Analogue of the Micromaser, *Phys. Rev. Lett.* **98**, 067204 (2007).
- [55] O. V. Zhirov and D. L. Shepelyansky, Synchronization and Bistability of a Qubit Coupled to a Driven Dissipative Oscillator, *Phys. Rev. Lett.* **100**, 014101 (2008).
- [56] A. Auffèves, D. Gerace, J.-M. Gérard, M. F. Santos, L. C. Andreani, and J.-P. Poizat, Controlling the dynamics of a coupled atom-cavity system by pure dephasing, *Phys. Rev. B* **81**, 245419 (2010).
- [57] N. V. Larionov and M. I. Kolobov, Analytical results from the quantum theory of a single-emitter nanolaser, *Phys. Rev. A* **84**, 055801 (2011).
- [58] K. An, J. J. Childs, R. R. Dasari, and M. S. Feld, Microlaser: A Laser with One Atom in an Optical Resonator, *Phys. Rev. Lett.* **73**, 3375 (1994).
- [59] K. An, Validity of single-atom approximation in the many-atom microlaser, *J. Phys. Soc. Jpn.* **72**, 811 (2003).
- [60] E. del Valle and F. P. Laussy, Regimes of strong light-matter coupling under incoherent excitation, *Phys. Rev. A* **84**, 043816 (2011).
- [61] S. André, P.-Q. Jin, V. Brosco, J. H. Cole, A. Romito, A. Shnirman, and G. Schön, Single-qubit lasing in the strong-coupling regime, *Phys. Rev. A* **82**, 053802 (2010).
- [62] P. Gartner, Two-level laser: Analytical results and the laser transition, *Phys. Rev. A* **84**, 053804 (2011).
- [63] T. B. Karlovich and S. Y. Kilin, Quantum statistical properties of one-atom lasers, *Opt. Spectrosc.* **91**, 343 (2001).
- [64] N. V. Larionov and M. I. Kolobov, Quantum theory of a single-emitter nanolaser, *Phys. Rev. A* **88**, 013843 (2013).
- [65] E. N. Popov and N. V. Larionov, in *Saratov Fall Meeting 2015: Third International Symposium on Optics and Biophotonics and Seventh Finnish-Russian Photonics and Laser Symposium (PALS)*, edited by E. A. Genina, V. V. Tuchin, V. L. Derbov, D. E. Postnov, I. V. Meglinski, K. V. Larin, and A. B. Pravdin, SPIE Proc. (SPIE, Bellingham, 2016), Vol. 9917, pp. 729–734.
- [66] J. Kim, D. Yang, S. Oh, and K. An, Coherent single-atom superradiance, *Science* **359**, 662 (2018).
- [67] M. A. Nielsen and I. Chuang, *Quantum Computation and Quantum Information* (Cambridge University Press, Cambridge, 2000).
- [68] E. Polino, M. Valeri, N. Spagnolo, and F. Sciarrino, Photonic quantum metrology, *AVS Quantum Sci.* **2**, 024703 (2020).
- [69] Y. Shih, *An Introduction to Quantum Optics: Photon and Biphoton Physics* (CRC, Boca Raton, 2018).
- [70] D. Mogilevtsev, A. Mikhalychev, V. S. Shchesnovich, and N. Korolkova, Nonlinear dissipation can combat linear loss, *Phys. Rev. A* **87**, 063847 (2013).
- [71] E. T. Jaynes and F. W. Cummings, Comparison of quantum and semiclassical radiation theories with application to the beam maser, *Proc. IEEE* **51**, 89 (1963).
- [72] K. E. Cahill and R. J. Glauber, Density operators and quasiprobability distributions, *Phys. Rev.* **177**, 1882 (1969).
- [73] K. E. Cahill and R. J. Glauber, Ordered expansions in boson amplitude operators, *Phys. Rev.* **177**, 1857 (1969).
- [74] U. M. Titulaer and R. J. Glauber, Correlation functions for coherent fields, *Phys. Rev.* **140**, B676 (1965).
- [75] L. Mandel, Non-classical states of the electromagnetic field, *Phys. Scr.* **1986**, 34 (1986).
- [76] C. T. Lee, Measure of the nonclassicality of nonclassical states, *Phys. Rev. A* **44**, R2775 (1991).
- [77] N. Lütkenhaus and S. M. Barnett, Nonclassical effects in phase space, *Phys. Rev. A* **51**, 3340 (1995).
- [78] M. Hillery, Conservation laws and nonclassical states in nonlinear optical systems, *Phys. Rev. A* **31**, 338 (1985).
- [79] T. Richter and W. Vogel, Nonclassicality of Quantum States: A Hierarchy of Observable Conditions, *Phys. Rev. Lett.* **89**, 283601 (2002).
- [80] E. Shchukin, T. Richter, and W. Vogel, Nonclassicality criteria in terms of moments, *Phys. Rev. A* **71**, 011802(R) (2005).
- [81] S. De Bièvre, D. B. Horoshko, G. Patera, and M. I. Kolobov, Measuring Nonclassicality of Bosonic Field Quantum States via Operator Ordering Sensitivity, *Phys. Rev. Lett.* **122**, 080402 (2019).
- [82] H. J. Carmichael, *Statistical Methods in Quantum Optics I: Master Equations and Fokker-Planck Equations* (Springer Science + Business Media, New York, 1999), Vol. 1.
- [83] J. N. Reddy, *An Introduction to the Finite Element Method* (McGraw-Hill, New York, 2006).
- [84] R. Horodecki and M. Horodecki, Information-theoretic aspects of inseparability of mixed states, *Phys. Rev. A* **54**, 1838 (1996).
- [85] N. J. Cerf and C. Adami, Quantum extension of conditional probability, *Phys. Rev. A* **60**, 893 (1999).
- [86] T. Tufarelli, A. Ferraro, A. Serafini, S. Bose, and M. S. Kim, Coherently Opening a High- $Q$  Cavity, *Phys. Rev. Lett.* **112**, 133605 (2014).
- [87] J.-I. Yoshikawa, K. Makino, S. Kurata, P. van Loock, and A. Furusawa, Creation, Storage, and On-Demand Release of Optical Quantum States with a Negative Wigner Function, *Phys. Rev. X* **3**, 041028 (2013).
- [88] P. Colman, P. Lunnemann, Y. Yu, and J. Mørk, Ultrafast Coherent Dynamics of a Photonic Crystal All-Optical Switch, *Phys. Rev. Lett.* **117**, 233901 (2016).
- [89] G. Chimczak, K. Bartkiewicz, Z. Ficek, and R. Tanaś, Creating a switchable optical cavity with controllable quantum-state mapping between two modes, *Sci. Rep.* **8**, 14740 (2018).
- [90] Z. Cheng, J. Dong, and X. Zhang, Ultracompact optical switch using a single semisymmetric Fano nanobeam cavity, *Opt. Lett.* **45**, 2363 (2020).
- [91] H. Qi, X. Wang, X. Hu, Z. Du, J. Yang, Z. Yu, S. Ding, S. Chu, and Q. Gong, All-optical switch based on novel physics effects, *J. Appl. Phys.* **129**, 210906 (2021).
- [92] Y. Yin, Y. Chen, D. Sank, P. J. J. O'Malley, T. C. White, R. Barends, J. Kelly, E. Lucero, M. Mariantoni, A. Megrant, C. Neill, A. Vainsencher, J. Wenner, A. N. Korotkov, A. N. Cleland, and J. M. Martinis, Catch and Release of Microwave Photon States, *Phys. Rev. Lett.* **110**, 107001 (2013).
- [93] W. J. Munro, K. Nemoto, G. J. Milburn, and S. L. Braunstein, Weak-force detection with superposed coherent states, *Phys. Rev. A* **66**, 023819 (2002).
- [94] C. W. Helstrom, Quantum detection and estimation theory, *J. Stat. Phys.* **1**, 231 (1969).